Editors' Suggestion

Dispersion of backward-propagating waves in a surface defect on a three-dimensional photonic band-gap crystal

Timon J. Vreman ,[1] Melissa J. Goodwin ,[1] Lars J. Corbijn van Willenswaard ,[1,2] William L. Barnes ,[3,1] Ad Lagendijk ,[1] and Willem L. Vos [1,*]

[1] *Complex Photonic Systems (COPS), University of Twente, 7500 AE Enschede, The Netherlands*
[2] *Mathematics of Computational Science (MACS), University of Twente, 7500 AE Enschede, The Netherlands*
[3] *Department of Physics and Astronomy, University of Exeter, Exeter EX4 4QL, United Kingdom*

(Received 10 February 2025; revised 28 August 2025; accepted 1 October 2025; published 20 October 2025)

We experimentally study the dispersion relation of waves in a thin quasi-two-dimensional (2D) defect layer with periodic nanopores that sits on a 3D photonic band-gap crystal made from silicon by CMOS-compatible methods. The nanostructures are probed by momentum-resolved broadband near-infrared imaging of *p*-polarized reflected light as a function of off-axis wave vectors. We identify surface defect modes at frequencies inside the 3D photonic band gap with a narrow relative linewidth ($\Delta\omega/\omega = 0.028$), which are absent in defect-free 3D photonic band-gap crystals. We calculate the dispersion of the states with relevant mode symmetries using a plane-wave-expansion supercell method, with structural parameters directly extracted from scanning electron microscope images. The calculated bands match very well with the measured data. The slope of the dispersion curves of the surface defect states is negative in one off-axis direction, corresponding to backward-propagating waves in that direction where the phase velocity and the group velocity point in opposite directions, as confirmed by finite-difference time-domain simulations. We also present a didactic and analytic model of a 2D grating sandwiched between vacuum and a negative real effective $\varepsilon' < 0$ that mimics the 3D photonic band gap. The model's dispersion agrees with the experiments and with the full theory and shows that the backward propagation is caused by the surface grating. We discuss possible applications, including a device that senses the output direction of photons emitted by embedded quantum emitters in response to their emission frequency.

DOI: 10.1103/jckd-3l5d

I. INTRODUCTION

There is a worldwide interest in completely controlling the propagation and emission of photons, a major goal of the field of nanophotonics [1–6]. An intriguing kind of control is the opportunity to have photons propagate preferentially in a thin quasi-two-dimensional (2D) sheet in space, where propagation in the third dimension is exponentially attenuated or otherwise somehow impeded. Such peculiar "flattened" light propagation is well known on a single interface between a dielectric (with $\varepsilon'_d > 0$) and a metal (with $\varepsilon'_m < 0$) [7], where surface plasmon polaritons occur [8–11], and on their double-interfaced counterparts [12]. A second way to confine light to 2D occurs on the surface of a 3D photonic band-gap crystal [13], where surface states occur [2,14] that have been observed in pioneering studies by Ishizaki *et al.* [15,16]. A third approach is to confine light to a thin single-mode waveguide formed by a line defect in a 2D slab photonic crystal, such as the famous W1 waveguide [17–19]. In these platforms, light has wave vectors exceeding those in free space ($|\mathbf{k}| \equiv k_0 > |\mathbf{k}_{\text{vac}}|$), i.e., outside the light cone, so that special in or outcoupling methods are needed to overcome the momentum mismatch, such as gratings or prisms.

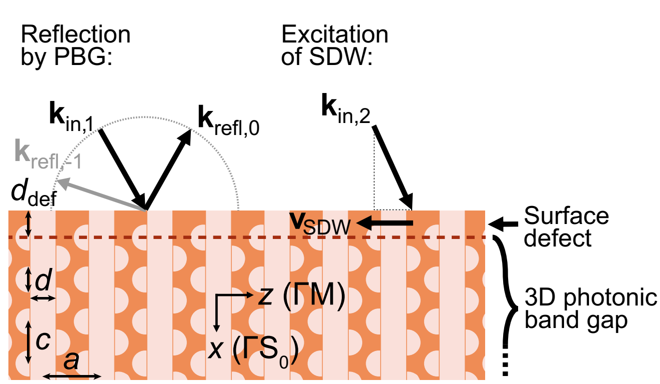

FIG. 1. Schematic cross section showing (left) the reflection of wave vector $\mathbf{k}_{\text{in},1}$ to $\mathbf{k}_{\text{refl},0}$ and higher-order diffraction $\mathbf{k}_{\text{refl},-1}$ by the 3D photonic band-gap crystal (pitches a and c and pore diameter d) and (right) the excitation of waves in a planar surface defect (thickness d_{def}). The surface defect wave (SDW) has a group velocity $\mathbf{v}_{\text{SDW}}$ pointing in the opposite direction as the z component of $\mathbf{k}_{\text{in},2}$. The x and z directions correspond to the directions ΓS_0 and ΓM of the irreducible Brillouin zone, respectively.

*Contact author: w.l.vos@utwente.nl; www.nano-cops.com

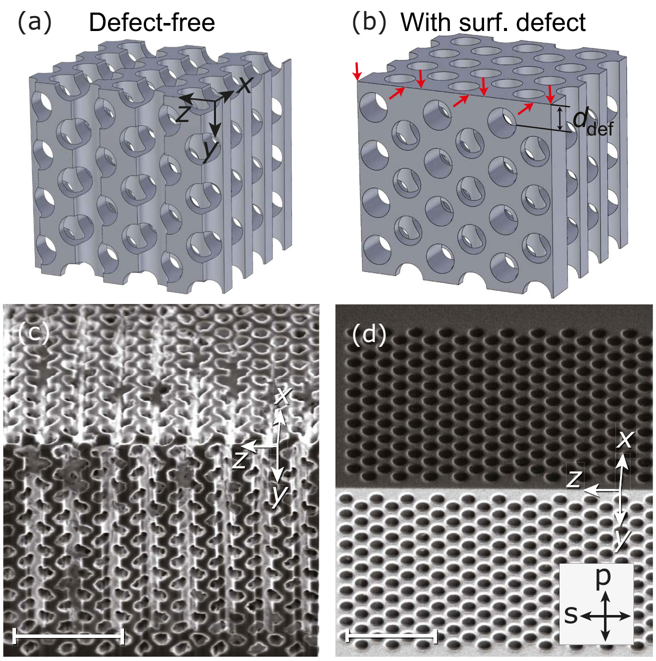

FIG. 2. Three-dimensional photonic band-gap crystals [(a)–(c)] without and [(b)–(d)] with surface defect. (a) Model of a periodic crystal which is periodic up to the crystal-to-air interface. (b) Model of the same structure, missing half-pores at the red arrows, creating a surface defect. (c) SEM image of the real photonic crystal after the surface was sliced off, similarly to (a). (d) SEM image of the mask of the same structure as (c) before the surface was sliced off, therefore having the surface defect, similarly to (b). Scale bars shown are 2 μm wide.

Here we study waves that propagate in a thin dielectric photonic layer on the surface of a 3D photonic band-gap crystal, as illustrated in the schematic in Fig. 1 (right). Such a thin layer may be viewed as a 2D surface defect on a 3D photonic band-gap crystal, which was recently proposed by our group as an effective absorber [20]. Since a 3D photonic band gap may be viewed as an effective medium with a negative real dielectric constant ($\varepsilon' < 0$), the light in the dielectric layer is exponentially attenuated into the lower half-space. In our case, the thin dielectric layer has a periodic array of pores. Therefore, our surface defect layer is structured, which may be conceived as a 2D slab photonic crystal, which plays the role of an incoupling or outcoupling grating for the light propagating inside the layer. Thus, our system operates inside the light cone, and the light in the surface defect layer is not strictly confined from free space [11], i.e., the modes are leaky. Our system may be compared to 2D slab photonic crystals, where leaky guided resonant modes are excited inside the light cone since they radiate in the third dimension [21,22]. The photonic crystal with a surface defect layer is shown in Figs. 2(b) and 2(d). For comparison, we also investigate a defect-free crystal where the surface defect is removed such that the structure is periodic up to the surface; see Figs. 2(a) and 2(c).

We probe the dispersion of the surface defect waves using momentum-resolved imaging [23–25] of the reflected light. Although the defect-free photonic crystal shows only high reflectivity at frequencies in the photonic band gap, the reflected light on the crystal with surface defect reveals narrow minima inside the high reflectivity of the band gap, indicating good confinement from free space. In addition, the minima are deep, indicating an efficient incoupling (∼90%) from free space. These properties are distinct from those of the approaches listed above that—in the visible part of the spectrum—often possess rather broad minima when excited within the light cone. In contrast to metal-based plasmonics, our system has a vanishing ε'', so we expect minimal nonradiative damping due to absorption. A second remarkable feature of our hybrid 2D + 3D system is that the waves reveal backward propagation [14,26–31], where the group velocity $\mathbf{v}_{\mathrm{SDW}}$ is opposite to $k_{\mathrm{in},z}$, see Fig. 1, as confirmed by simulations. The backward propagation results from the scattering of incident light by the periodically structured surface layer, as borne out by an analytic model that involves a surface grating on top of a negative ε band-gap medium.

To interpret our experiments, we performed plane-wave expansion calculations with supercells and find that the surface defect allows for predominantly *p*-polarized light to excite a surface defect wave that propagates inside the added dielectric material at frequencies matching the photonic band gap. The calculated dispersion agrees very well with the measured dispersion, which is exhilarating because all parameters are directly extracted from SEM images. We conclude our paper by discussing a few potential device applications.

II. DESIGN UNDER STUDY

A. Crystal structure in real space

Our 3D photonic band-gap crystals have the inverse woodpile crystal structure [32]. Inverse woodpile crystals have a broad 3D photonic band gap because of their cubic diamond-like structure [33]. We wish to find the smallest unit cell that describes the inverse woodpile structure. In previous work [34–39], an orthorhombic unit cell was used for convenience, but this unit cell is not primitive; hence, spurious artifacts occur in the band structures, such as the folding of bands. Instead, we here use the primitive unit cell, specifically a body-centered tetragonal (BCT) unit cell with conventional unit vectors. The unit cell is shown in Fig. 3(a), and the unit vectors are given by

$$\begin{aligned}\mathbf{a}_1 &= -\frac{a}{2\sqrt{2}}\hat{\mathbf{x}} + \frac{a}{2\sqrt{2}}\hat{\mathbf{y}} + \frac{a}{2}\hat{\mathbf{z}},\\ \mathbf{a}_2 &= \frac{a}{2\sqrt{2}}\hat{\mathbf{x}} - \frac{a}{2\sqrt{2}}\hat{\mathbf{y}} + \frac{a}{2}\hat{\mathbf{z}},\\ \mathbf{a}_3 &= \frac{a}{2\sqrt{2}}\hat{\mathbf{x}} + \frac{a}{2\sqrt{2}}\hat{\mathbf{y}} - \frac{a}{2}\hat{\mathbf{z}}.\end{aligned} \tag{1}$$

The 3D structure has pores in the x and y directions [40]. The space group of the structure is 141 [41]; see the Bilbao crystallographic server [42]. To have the same basis for symmetry operations as the Bilbao server, we position the pore along the x direction at $y = \frac{a}{4\sqrt{2}}$ and $z = \frac{a}{4}$, the pore along the y direction at $x = z = 0$, and repeat the pores at other positions inside the unit cell using the lattice vectors given in Eq. (1).

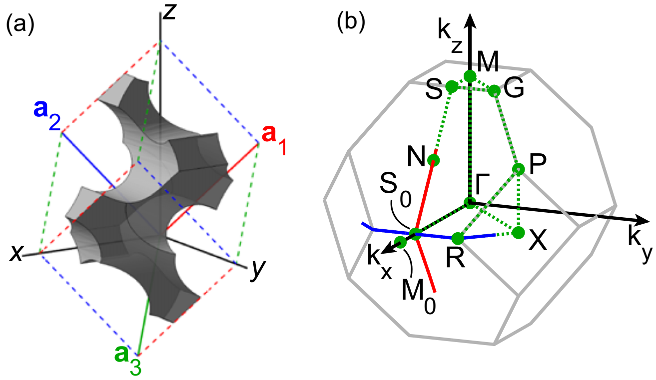

FIG. 3. (a) Unit cell of the inverse-woodpile structure. In dark gray, the silicon structure is shown. The pore's material, air, is not shown here. The unit vectors and pores' positions are defined in the text. (b) Green dotted: Irreducible Brillouin zone for a 3D photonic band-gap crystal with the inverse-woodpile structure. Gray: First Brillouin zone. Blue and red: Trajectories in **k**-space along which we computed bands to compare to the experiment. The trajectories extend until $k_y/|\mathbf{k}| = k_z/|\mathbf{k}| = \mathrm{NA} = 0.85$ for $\tilde{\nu} = 10^4\ \mathrm{cm}^{-1}$.

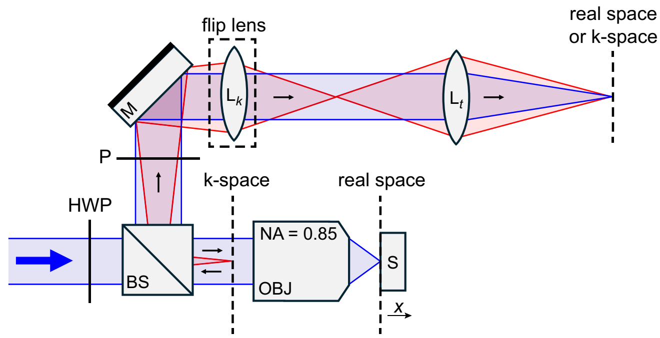

FIG. 4. Optical setup to measure spectrally resolved reflectivity both in real space and in wave vector space at the detector plane (vertical dashed line, top right). The incident beam has a tunable wavelength between 1000 and 1700 nm. The blue beam path pertains to real-space imaging of the sample. The red beam path pertains to imaging in wave-vector space (**k**-space). Components shown: a flip lens (L_k), a beam splitter (BS), an objective (OBJ), a sample (S), a mirror (M), a half-wave plate (HWP), a polarizer (P), and a tube lens (L_t).

B. Reciprocal lattice

From the unit vectors in 3D real space, we obtain the reciprocal lattice vectors that span 3D reciprocal space,

$$\mathbf{b}_1 = \frac{2\pi}{a}[\sqrt{2}\hat{\mathbf{y}} + \hat{\mathbf{z}}],$$

$$\mathbf{b}_2 = \frac{2\pi}{a}[\sqrt{2}\hat{\mathbf{x}} + \hat{\mathbf{z}}],$$

$$\mathbf{b}_3 = \frac{2\pi}{a}[\sqrt{2}\hat{\mathbf{x}} + \sqrt{2}\hat{\mathbf{y}}]. \qquad (2)$$

A general reciprocal lattice vector is given by

$$\mathbf{G} = f\mathbf{b}_1 + g\mathbf{b}_2 + h\mathbf{b}_3, \qquad (3)$$

where $f, g, h \in \mathcal{Z}$. The component parallel to the yz surface determines the reflected orders in Fig. 1(a) [43,44] and is given by

$$\mathbf{G}_\parallel = p\frac{2\pi}{c}\hat{\mathbf{y}} + m\frac{2\pi}{a}\hat{\mathbf{z}}, \qquad (4)$$

where $p, m \in \mathcal{Z}$, and $c \equiv a/\sqrt{2}$.

The commonly used irreducible Brillouin zone (IBZ) of the BCT lattice is shown in Fig. 3(b). It is instructive to rotate the IBZ 180° around the NP line. The rotated IBZ is one of the IBZs next to the nonrotated one, the unit cells together forming a triangular prism. The procedure maps S_0 to S, R to G, and M to M_0, the latter positioned at $\frac{4}{3}S_0$. The coordinates of the high-symmetry points of the IBZ and a calculated band structure are provided in Appendix A.

III. EXPERIMENTAL SECTION

A. Samples

Our photonic crystals are made of silicon by CMOS-compatible means. The inverse woodpile structure consists of two identical arrays of pores with radius R running in the perpendicular x and y directions. Each array of pores has a centered-rectangular structure with lattice constants a and c in a ratio $a/c = \sqrt{2}$ to ensure a cubic crystal structure. Here we use $a = 680$ nm and a pore diameter $d = 300$ nm to produce a photonic band gap in the near infrared and telecom ranges [35,36,38,39]. The pore arrays on the yz surface have an offset $\Delta z = a/4 = 170$ nm in the z direction compared to the xz surface, see Fig. 2.

The 3D silicon photonic crystals are made by etching deep cylindrical pores on the edge of a silicon beam in the x and y directions. We made the nanostructures using techniques we have described before [35,45,46]. In our standard mask-making procedure [45] we came to realize that we introduce a peculiar surface termination: from half of the pores at the xz and yz surfaces, the lower half of the pore is missing compared to a perfectly periodic structure that is terminated halfway through the pore, as in, e.g., Refs. [36,47]. Therefore, our fabricated structures have from the outset a surface defect; see Figs. 2(b) and 2(d). The thickness of the surface defect in Fig. 2(d) is $d_{\mathrm{def}} = 320 \pm 10$ nm, where d_{def} is defined as the distance from the surface to the centers of the pores closest to the surface. After experiments on the structure with a surface defect are completed, we carefully removed part of the surface of the photonic crystal with a focused ion beam (FIB) to realize the defect-free structure; see Figs. 2(a) and 2(c). Similar measurements were repeated on a second photonic crystal both with and without surface defect, see Appendix D, and were found to reproduce very well.

B. Optical setup

Although band gaps and surface defects are typically studied by scanning the angle of incident light [15,16,24,48–54], we chose to scan the frequency while directly imaging the reflectivity as a function of $\mathbf{k}_\parallel$, a method called momentum-resolved imaging or Fourier imaging [24,24,25,55–57]. Figure 4 schematically shows our setup to collect spectrally resolved reflectivity in both real and wave-vector space. Our setup is based upon that used in Refs. [38,58]. Briefly, linearly polarized light from a supercontinuum white light source (Fianium SC-400-2) is spectrally filtered by a monochromator with spectral resolution $\Delta\lambda = 0.6$ nm (Oriel MS257), collimated, and set to p-polarized light by a half-wave plate. Waves traveling in the x direction are labeled as p-polarized if the **E** field is oscillating parallel to the pores along the y axis. The beam is focused ($\phi < 2$ μm) on the samples with an objective (Olympus LCPLN100XIR) with a numerical aperture NA = 0.85. Reflected light is collected in backscatter geometry by the same objective and directed via a beam splitter through a p-polarized polarizer to an InGaAs camera (Photonic Sciences). To collect spectral information in **k**-space, light collected with the objective is collimated, and the back focal plane is imaged by two lenses (flip lens and tube lens, 300 and 500 mm, respectively) onto a camera. A frequency scan in **k**-space of 160 data points takes 5 min per sample.

C. Experimental details

The reflectivity is normalized relative to the reflectivity measured with a gold mirror, assuming $R_{\mathrm{Au}} = 96\%$ reflectivity. The maximum accessible k_y and k_z, also known as the light cone, is equal to the NA times the magnitude of the wave vector in air k_0, i.e., $k_{\parallel,\max} = (\mathrm{NA})k_0$.

Each measurement run yields a 3D dataset—two dimensions are spatial (k_y and k_z) and one is the frequency ($\tilde{\nu}$). Videos in the Supplemental Material show whole datasets Refs. [59,60], also for a second photonic crystal with the same design parameters [61,62]. For simplicity, here we will focus on either one frequency (two spatial dimensions) or we will set $k_y = 0$ or $k_z = 0$ (one spatial and one frequency dimension).

D. Photonic band-structure calculations

We determine the edges of the 3D photonic band gap of the crystal without defect as a function of $\mathbf{k}_\parallel$ for p-polarized light as follows: The band structures for Bloch modes are calculated for wave vectors on the boundary of the first Brillouin zone, see Fig. 3(b), as those wave vectors typically determine the frequency edges of the band gap [63]. The ΓS_0 direction corresponds to waves incident from the normal x direction. By setting $k_y = 0$ or $k_z = 0$, two paths are defined along the first Brillouin zone boundary; see the red and blue lines in Fig. 3(b), respectively. Modes with **k** vectors along the red and blue lines are calculated using the MIT Photonic Bands (MPB) open-source software [64], using a pore diameter $d = 300$ nm and lattice parameter $a = 680$ nm (reduced pore radius $r/a = 0.22$).

Bloch modes in a photonic crystal have symmetry properties [1], which we also calculate using the MPB software. The symmetry properties of modes with wave vectors along the ΓS_0 path are categorized into four types, namely Σ_1 to Σ_4 [42,65], as elaborated on in Appendix B. These wave vectors correspond to plane waves incident from the x direction. Due to the symmetry properties of polarized plane waves, s-polarized and p-polarized waves excite only modes from Σ_3 and Σ_4, respectively. In the band structures, we only show the modes with the symmetry corresponding to the polarization of that measurement. We also do this for the off-axis modes, as the symmetry properties are expected to still dominate.

E. Angle of reflection off photonic crystals

For a planar mirror, the angle of incidence equals the angle of reflection due to the conservation of the parallel component of the wave vector: The incoming $\mathbf{k}_{\mathrm{in},\parallel}(\tilde{\nu})$ equals the outgoing $\mathbf{k}_\parallel(\tilde{\nu})$ at a certain wave number $\tilde{\nu}$ [66]. Furthermore, a mirror reflects all angles (almost) equally.

The interface between air and a 3D photonic band-gap crystal is more complex [2,43,44,67]. If an incident wave with $\mathbf{k}_{\mathrm{in},\parallel}(\tilde{\nu})$ excites a Bloch mode, then the reflection of that incident wave will be low; see Fig. 1 (right). And if such an incident wave does not excite a Bloch mode, then it is reflected by the 3D band gap, see Fig. 1 (left). In addition to the specularly reflected light, diffraction orders may occur due to the periodicity at the surface of a photonic crystal, as described by $\mathbf{G}_\parallel$ in Eq. (4). Analysis of the reflected waves is easiest in the regime where only the specularly reflected light is collected by the objective's acceptance cone. The boundary of this regime is calculated as follows: the $(p = 0, m = -1)$ diffraction order is illustrated in Fig. 1 (gray arrow). Together with the $(p = 0, m = 1)$ order, this is the diffraction order that the objective collects soonest because it has the lowest $|\mathbf{G}_\parallel|$. We start collecting diffraction orders when $\mathbf{k}_{\mathrm{in}}$ and the reflected $\mathbf{k}_{-1}$ both overlap with the maximum angle of the objective. In other words, only specularly reflected light is collected when $k_{\mathrm{in},z} = -k_z = \min(|\mathbf{G}_\parallel|)/2 = \frac{\pi}{\mathrm{a}} \geqslant k_0(\mathrm{NA}) = 2\pi\tilde{\nu}(\mathrm{NA})$, i.e., when $\tilde{\nu} \leqslant 8650$ cm^{-1}. For modes on the axis $k_y = k_z = 0$, no higher diffraction orders are collected when $\tilde{\nu} \leqslant 17300$ cm^{-1}. Hence, in the frequency region of the band gap and below, we collect no reflection from higher diffraction orders.

We interpret our experimental observations with Bloch modes calculated for the infinite crystal as follows [68]. The Bloch modes calculated inside the photonic crystal are refracted at the crystal-to-air interface, possibly with multiple diffraction orders in air. Given the periodicity at the surface is the same [see Eq. (4)], the analysis of the refraction orders is the same as for the reflected diffraction orders, i.e., we only collect the zeroth order in the frequency region of the band gap and below. Therefore, the calculated band structures are plotted directly onto the experimentally obtained wave number versus $\mathbf{k}_\parallel$ graphs. Due to the periodicity, only bands inside the first Brillouin zone need to be considered [44].

F. Finite-difference time-domain simulation

The excitation of the surface defect mode is simulated on an ideal 3D photonic crystal of $6c \times 5c \times 40a$ with a surface defect with thickness $d_{\mathrm{def}} = 320$ nm. In finite-difference time-domain simulations (FDTD) using open-source package Meep [69], a p-polarized quasimonochromatic plane wave with $k_z = +2.0$ μm^{-1} and $\tilde{\nu} = 6500$ cm^{-1} is incident on the photonic crystal, which corresponds to the $\mathbf{k}_{\mathrm{in}}$ that excites the surface defect mode. The simulation domain is surrounded by 1.5 μm of perfectly matched layer to absorb outgoing waves. Cross sections of the

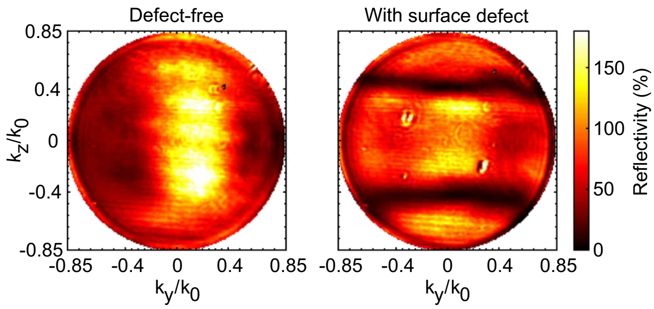

FIG. 5. Momentum-resolved image of the reflectivity of the photonic crystal (left) without and (right) with defect at $\tilde{\nu} = 6850$ cm^{-1} ($\lambda = 1460$ nm; $a/\lambda = 0.4657$) for p-polarized light. We observe high reflectivity from the band gap with strong linelike troughs from the defect mode. The NA of the objective determines the maximum $|\mathbf{k}_\parallel|/k_0 \leqslant 0.85$.

electric field in the xz plane are extracted from the simulation to show the propagation of the guided wave.

G. Supercell calculation of the surface defect mode

To calculate the dispersion of the surface defect mode, we apply the supercell method [70]. For this calculation, the orthorhombic unit cell is used, as previously used [34,36,38,39,71], with the pores at the same position as in Sec. II A. Six unit cells of 3D photonic crystal are alternated with six unit cells of air in the x direction, with a resolution of $192 \times 16 \times 23$. Of the outer two unit cells, one has a surface defect with thickness $d_{\text{def}} = 320$ nm, and the other has proper surface termination halfway through the pores. A schematic of the supercell is shown in Fig. 14(a) of Appendix C.

Modes are calculated at $\mathbf{k}$ vectors with either $k_y = 0$, or $k_z = 0$ while keeping k_x constant. Next to the surface defect mode and bulk crystal modes, the supercell method also finds modes in the air unit cells, which interact with and obscure the surface mode. The confinement of the surface defect modes near the surface and the dominant polarization of the defect mode are used to isolate the surface defect mode, as elaborated on in Appendix C.

IV. RESULTS

A. Reflectivity at a single frequency

The momentum-resolved reflectivity of p-polarized light is shown in Fig. 5 at a frequency ($\tilde{\nu} = 6850$ cm^{-1}) deep inside the band gap. Without the surface defect, the reflectivity is high, as expected from a complete 3D band gap. In the k_z direction, the reflectivity is high everywhere; in the k_y direction, the reflectivity is greater than 100% near $k_y = 0$ and lower at $|k_y| > 0$. We discuss the reason for the directional reflectivity exceeding 100% in Sec. V. The reflectivity is centered slightly towards positive k_y, as the surface removal process by the FIB results in a small angular offset. Other than that, the reflectivity is symmetric around both $k_y = 0$ and $k_z = 0$, as expected from a symmetric structure.

For the crystal with the surface defect, we also observe high reflectivity, and the reflectivity is mostly symmetric around $k_y = 0$ and $k_z = 0$. Remarkably, we observe two deep troughs,

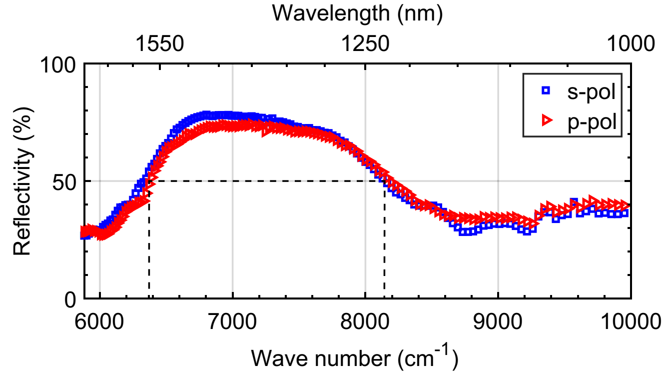

FIG. 6. Total reflectivity of the 3D photonic band-gap crystal without surface defect, as shown in Fig. 2(c). Blue data are for s-polarization, red data for p-polarization. Horizontal dashed line indicates the half height and vertical dashed lines indicate the full width at half maximum. Wave number $\tilde{\nu} \equiv \omega/2\pi c_0$.

tending to a minimum reflectivity as low as ~10%, resulting from the surface defect. The troughs are shaped like two lines: They extend along all probed k_y, and they are sharp along k_z appearing at $|k_z| = 0.4k_0$. As a function of increasing frequency, the troughs from Fig. 5 approach each other, as is observed in the video of the whole momentum-resolved dataset in the Supplemental Material Ref. [60].

Since the minima are absent in the reflectivity acquired from the sample without a defect, we conclude that they correspond to new states from the surface defect. The minima correspond to the excitation of waves that travel between the band gap and air, as illustrated in Fig. 1. Because the wave is excited with light inside the light cone, radiation into the air is expected. We further investigate and discuss the radiation in Secs. IV D and V.

B. Frequency-resolved reflectivity of 3D band gap

By integrating the reflectivity over $\mathbf{k}_\parallel$, we obtain real-space reflectivity spectra, similarly to previous studies in our group [38,39], and elsewhere [53,72,73]. The total reflectivity spectra measured on the structure without defect in Fig. 6 reveal broad and intense peaks centered at $\tilde{\nu}_c = 7200$ cm^{-1} for both polarizations with maxima up to 70–80%, confirming the high quality of our crystal structures. The peaks are broad with widths (full width at half maximum) of about $\Delta\tilde{\nu}_c = 1800$ cm^{-1}, corresponding to a relative bandwidth of $\Delta\tilde{\nu}_c/\tilde{\nu}_c = 25\%$ and thus confirming the expected high photonic strength of these high-index-contrast silicon-air nanostructures [38,39]. The reflectivity spectra are smooth for both polarizations. The band gap is expected to extend until 8200 cm^{-1} (see the band structure in Fig. 11), but we observe that the reflectivity starts to decrease at 7800 cm^{-1}, which we attribute to minor manufacturing defects, such as noncylindrically shaped pores.

We now turn to the frequency- and momentum-resolved reflectivity spectra for p-polarized light. To keep the representation of the large datasets tractable, we plot in Fig. 7(a) cross sections through the momentum-resolved data at $k_y = 0$ (left) and $k_z = 0$ (right). In the $k_y = 0$ plane, the reflectivity is high for all probed k_z and symmetric about $k_z = 0$. With increasing

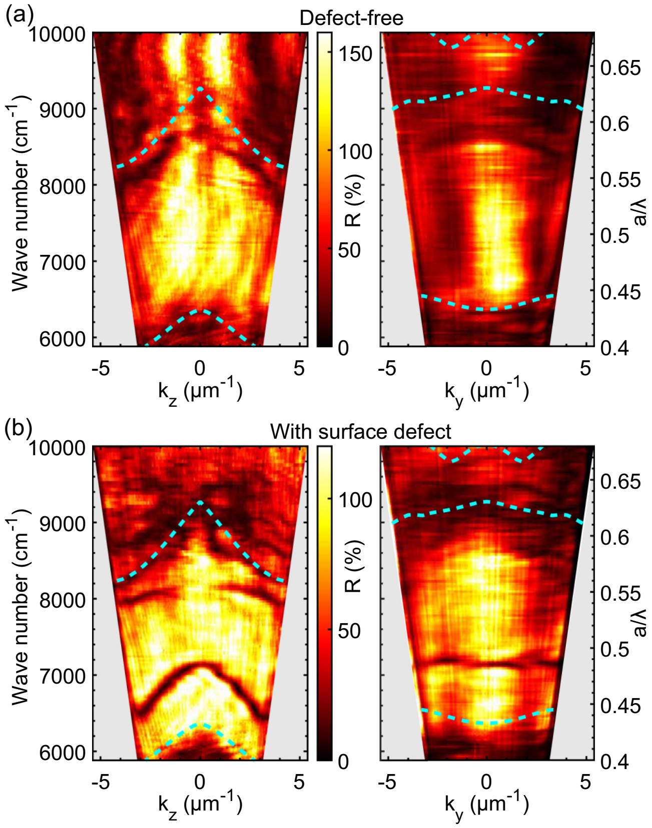

FIG. 7. Momentum-resolved reflectivity R for p-polarized light of a 3D photonic crystal (a) without and (b) with a surface defect. Samples without and with a surface defect are shown in Fig. 2. Gray area: Outside the objective's illumination cone. Cyan, dashed: Symmetry-selected bands calculated along the red and blue lines in Fig. 3(b) for pore diameter $d = 300$ nm. The region between these regular bands shows high reflectivity from the band gap, where the troughs inside the high reflectivity represent the defect mode.

frequency to about 8000 cm^{-1}, low reflectivity appears at $|k_z| = 3$ μm^{-1} that we attribute to the upper edges of the band gap, also referred to as "air" bands [2]. Furthermore, decreased reflectivity appears at even higher frequencies, which we interpret as higher bands above the gap.

In the $k_z = 0$ plane in Fig. 7(a) (right), we observe a high reflectivity for momenta central near $k_y = 0$, whereas the reflectivity decreases for $|k_y| > 1$ μm^{-1}. A directional reflectivity that apparently exceeds 100% is discussed in Sec. V.

Figure 7 also shows (dashed cyan) bands calculated at the boundary of the first Brillouin zone; see the red and blue lines in Fig. 3(b). The bands shown here are selected according to whether they can be excited with incident p-polarized light based on their dominant symmetry type. Below the gap, the bands and reflectivity match well. Above the gap, the shapes of the calculated modes match the shape of the measured band gap well, but the frequency of the calculated modes is greater than in the experiment for a straightforward reason: The lowest frequency of the first mode above the band gap occurs not at S_0 but slightly inside the FBZ, as is seen by the frequencies of the modes calculated along ΓM_0 in Fig. 13.

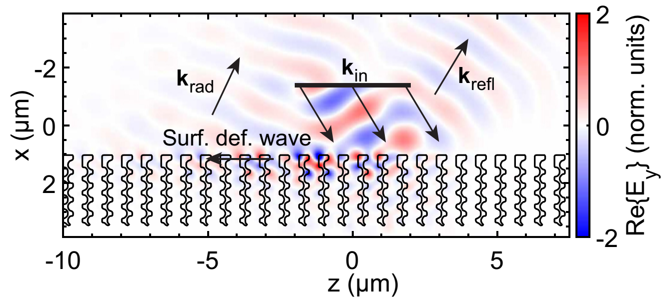

FIG. 8. Two-dimensional slice of a 3D FDTD simulation, with the real part of the electric field in the y direction (Re$\{E_y\}$). At the rectangular source (black horizontal bar), a continuous wave with wave number $\tilde{\nu} = 6500$ cm^{-1} is created at the defect frequency and with wave vector $\mathbf{k}_{\text{in}}$. The wave is incident on the photonic crystal with surface defect layer (black curves, layer at $x = -1$ μm). The incident wave excites a surface defect wave in the $-z$ direction, which radiates in the direction $\mathbf{k}_{\text{rad}}$. The incident wave is also reflected by the 3D band gap to $\mathbf{k}_{\text{refl}}$.

C. Frequency-resolved reflectivity of 3D band gap with surface defect

In Fig. 7(b), we plot the cross sections of momentum-resolved reflectivity for a 3D photonic band-gap crystal with a surface defect [see Figs. 2(b) and 2(d)]. The left panel is a $k_y = 0$ cross section and the right panel a $k_z = 0$ cross section. Similarly to the crystal without a defect, the spectra are symmetric in $k_z = 0$ and $k_y = 0$, respectively. They are even more symmetric than without defect since fewer manufacturing steps are involved.

A striking feature in Fig. 7(b) is a deep trough inside the band gap. In the $k_y = 0$ cross section (left), the trough runs from 6500 to 7050 cm^{-1}, whereas the $k_z = 0$ cross section (right) is nearly constant at 7050 cm^{-1}. The width of the mode is about $\Delta\tilde{\nu} = 200$ cm^{-1}, which corresponds to a relative bandwidth $\Delta\tilde{\nu}/\tilde{\nu} = 0.028$. The surface defect mode's dispersion is directly given by the shape of the troughs in these plots and is very different between k_z and k_y: k_z strongly impacts the energy required to excite a surface defect mode, while k_y hardly does. The group velocity is given by $\nabla_{\mathbf{k}}\omega$ [2], where $\omega = 2\pi c_0\tilde{\nu}$. Given that the frequency of the surface defect mode decreases as a function of increasing $|k_z|$, we expect the wave to travel in the opposite direction as $k_{\text{in},z}$. Since the dispersion as a function of k_y is relatively flat, we expect slow propagation in the y direction.

D. Simulations of the surface defect waves

Figure 8 shows one snapshot of the FDTD simulations to visualize waves in the surface defect in real space, taken after 55 wave periods. The simulations show that a plane wave at +30° incidence is partly reflected towards $\mathbf{k}_{\text{refl}} \equiv \mathbf{k}$ by the 3D band gap and partly excites a wave that travels between on one side the band gap and on the other air. From the decay of the $\mathbf{E}$ field as a function of x, we estimate the penetration depth due to the band gap, also known as the Bragg length, to be $l_{\text{Br}} = 700 \pm 50$ nm, which corresponds to an effective permittivity of the photonic crystal at frequencies in the band gap of about $\varepsilon = -0.12$.

The wave travels in the $-z$ direction, which is consistent with the measured dispersion in Sec. IV C. It is striking that $k_{\mathrm{in},z}$ is positive (like in Fig. 1) while the wave's energy travels to the left, i.e., the group velocity of the wave is negative [2,74]. We then conclude that we observe a backward-propagating wave on the surface of a 3D photonic band-gap crystal along the k_z direction. In the video in the Supplemental Material Ref. [75], we observe that the group velocity of the surface defect wave is slow compared to that of the reflected wave.

The surface defect wave radiates, and from the simulations we find it has a propagation length of ~ 3 µm. This is a useful start for applications, especially since various improvements can be envisaged; see Sec. V. The radiation travels in the $+z$ direction, in (almost) the same direction as $\mathbf{k}$. That is expected: In Sec. IV B we found that $k_{\mathrm{in},z} = k_z$, and due to conservation of parallel momentum $k_{\mathrm{SDW},z} = k_{\mathrm{in},z} + m\frac{2\pi}{a} = k_{\mathrm{rad},z} + p\frac{2\pi}{a}$, where $\{m, p\} \in \mathcal{Z}$. For $\mathbf{k}$ and $\mathbf{k}_{\mathrm{in}}$ to both be in the light cone, $k_{\mathrm{in},z} = k_{\mathrm{rad},z}$. Therefore, we conclude that $k_z = k_{\mathrm{rad},z}$.

The $\tilde{\nu}_{\mathrm{SDW}}$ that excites a surface defect mode at $k_z = 2.0\ \mu\mathrm{m}^{-1}$ in the simulation is 270 cm^{-1} lower than in the experiment, which we attribute to the absence of manufacturing defects in Ref. [76] and the limited resolution of the simulation.

While not shown here, in the y direction, the wave hardly propagates near $|k_y| = 0$, as expected from the measured dispersion along k_y. Additional simulations show that at normal incidence ($k_y = k_z = 0$), the wave propagates in both $\pm z$ directions.

E. Calculated dispersion via supercell method

Using the supercell method, we calculate the dispersion of the surface defect mode for the inverse woodpile with surface defect of $d_{\mathrm{def}} = 320$ nm. Next to surface modes, the supercell method also provides bulk crystal and air modes, which are undesired here. By setting requirements on the symmetry properties and confinement of the mode at the defect interface, we were able to isolate and reconstruct the dispersion of the defect mode, as further elaborated on in Appendix C. We directly plot the (green dashed) calculated dispersion onto the measured data in Fig. 9 (see Sec. III E). The shape of the calculated dispersion matches very well with the measured dispersion, confirming the experimental results and theoretical analysis. The defect mode is remarkably sensitive to the defect thickness d_{def}: A change of d_{def} from 320 to 240 nm shifts the calculated defect frequency at $k_z = k_y = 0$ from 7060 to 7800 cm^{-1} (Fig. 14).

V. DISCUSSION

A. Didactic model

The dispersion of the waves in the surface defect of the photonic crystal corresponds very well to the measured dispersion, but the good agreement in itself does not yet provide a physical argument as to why the waves are backward-propagating. To address this question, we propose an analytic model of Fresnel reflectivity of unstructured media for p-polarized light. The model simplifies our experimental configuration by considering only three media, namely:

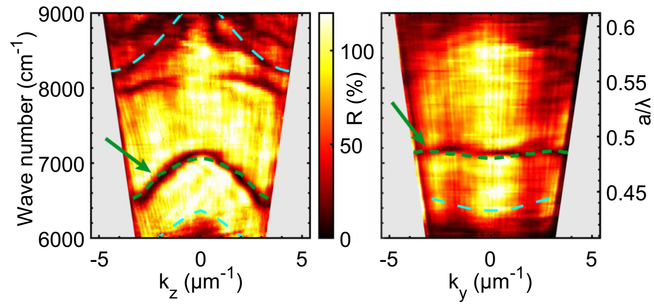

FIG. 9. Zoom-in of Fig. 7(b) showing the momentum-resolved reflectivity R (colors in the color bar in the center) with (in green) the surface defect mode calculated with the supercell method.

(i) An upper half-space consisting of air, with a real dielectric constant $\varepsilon_1' = 1$,

(ii) A defect layer with a real dielectric constant ε_2' and a thickness $d_{\mathrm{def}} = 320$ nm,

(iii) A lower half-space consisting of a photonic band gap described by a negative real dielectric constant [2,28,37] equal to $\varepsilon_3' = -0.12$ [77].

For the defect layer, we estimate the effective dielectric constant from a volume average of the refractive indices of air and silicon to be $\varepsilon_2 = n_{\mathrm{eff}}^2 = 2.4^2$. The 3D photonic band gap is modeled with an effective dielectric constant that we take to be *negative* and *real*. The defect layer acts like a core in a low-ε cladding of a waveguide. The (black) waveguide modes exist outside the ($m = 0$) light cone.

Subsequently, we incorporate the effects of periodicity from the pores at the surface (illustrated in Fig. 1) using a grating with spacing a such that $k_{\mathrm{in},z}$ also creates cones at $m\frac{2\pi}{a} = m \times 9.24\ \mu\mathrm{m}^{-1}$ for $m \in \mathbb{Z}$, see the blue lines in Fig. 10 for $m = \pm 1$. The off-shell modes of $m = \pm 1$ represent

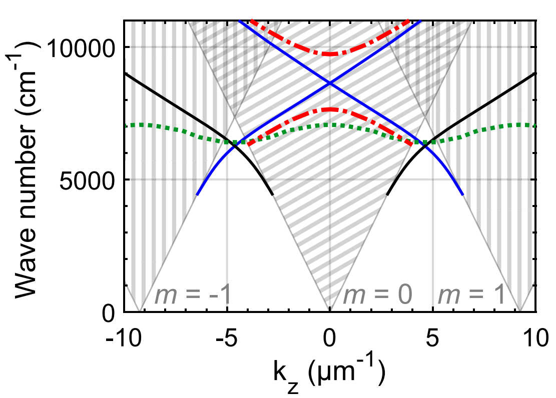

FIG. 10. Calculated dispersion of modes in a didactic Fresnel model of three media and a grating with orders $m = -1, 0, 1$. Parameters of the model are defined in the text. Diagonal striped fill: Light cones of $m = 0$ and $m = \pm 1$. Solid lines: Calculated modes for (black) $m = 0$ and (blue) $m = \pm 1$. The calculated modes start from the edge of a light cone. Green dotted: Supercell computations along k_z from Fig. 9 (left). Red: Hyperbola originating from an avoided crossing of the blue $m = \pm 1$ modes.

backward waves below $\tilde{\nu} < 8600\ \mathrm{cm}^{-1}$ inside the light cone of $m = 0$, as can be seen from their negative slope of the dispersion curve in the k_z direction.

In the model, the $m = \pm 1$ modes cross without interaction, but in reality, an avoided crossing is expected, which is taken into account by plotting a hyperbola with as asymptotes the $m = \pm 1$ modes; see the red line. The opening $\Delta\tilde{\nu}$ at $k_z = 0$ is estimated using Eq. 2.11 of Ref. [78] for a 2D structure with $\mathbf{G} = 4\pi/c\hat{\mathbf{z}}$. Given the simplicity of the model, the hyperbola matches well with the supercell calculations at low $|k_z|$. At high $|k_z|$ the model's derivative does not tend to zero and thus the agreement with the supercell calculation is worse, which is reasonable as the effective medium approach of the defect layer is poorer for increasing $|k_z|$.

Along the y direction, the grating spacing is $a/\sqrt{2}$, which means the light cones are further apart and no grating effects are visible inside the frequency region of the band gap explored here. Indeed, we do not observe a backward wave along the y direction in our simulations.

B. Further discussion

First, let us discuss the trade-off between ease of excitation of and amount of radiation by the surface defect wave. Using waves inside the light cone, we excite waves that radiate back into the air more readily than fully confined waves. For certain applications, less radiation and more confinement may be desired. By increasing the confinement threshold to 80% in the supercell computations, we find two strategies to improve the confinement: (1) Confinement is enhanced by exciting (the same or other) bands at a $\sqrt{k_y^2 + k_z^2}$ outside the light cone, e.g., by using a prism [11,15], and (2) by exciting surface modes with symmetry Σ_1 and Σ_2, which do not couple easily to outside waves.

Second, the question arises as to why we do not observe any defects in Fig. 7(a), where despite $d_{\mathrm{def}} = 0$ there is still a surface termination. The reason is that there are no surface defect states in the band gap, which follows from the same calculations as in Sec. IV E with a confinement restriction at the bottom surface (which has defect width $d_{\mathrm{def}} = 0$).

Third, let us consider the observation of more than 100% reflectivity in Fig. 5 (left) and Fig. 7(a) (right). Detection of more than 100% *directional* reflectivity at particular $\mathbf{k}$ is not against conservation of energy; it is the *total* reflectivity integrated over all $\mathbf{k}$ that must stay below 100%, which it does (see Fig. 6). More than 100% directional reflectivity implies that multiple $\mathbf{k}_{\mathrm{in}}$ are reflected toward the same $\mathbf{k}$, even at frequencies in the band gap. However, such redirection is unexpected from Refs. [1,2,44,67] because they only find redirection in the form of diffraction orders with a discrete $\mathbf{G}_{\parallel}$ that, for our sample and surface, only occurs at frequencies above the band gap, see Sec. III E. A stark difference between our experiment and the situations described in Refs. [1,2,44,67] is that we consider focused light while they consider plane waves. While plane waves probe an in theory infinite surface, our sharp focus only probes a few square micrometers. It is known that the $\mathbf{k}_{\parallel}$ provided by diffraction gratings—also periodic structures—is not as well defined when probing only a few lines [79]. Therefore, and potentially due to other yet unknown reasons, the previous theoretical work and simulations on the reflection of plane waves may not directly be applicable to our experiment. To study the reflectivity with a sharp focus outside the laboratory, we perform a momentum-resolved FDTD simulations in Appendix E. The results of the simulations corroborate our experiments.

Fourth, we remark that we have not studied cross-polarization coupling from p- to s-polarized light since the polarizer in front of the camera filters out s-polarized light.

Fifth, we discuss potential applications of a photonic crystal with such a surface defect. Our hybrid system between a waveguide and a surface wave may not only have the usual "flat light" applications in (bio)sensing and photonic communication but also completely new applications that profit from the 3D band gap (cavity quantum electrodynamics including spontaneous emission inhibition) combined with a tunable wave vector (hence: tunable directionality) that is set by the emission frequency. For example, say we put a quantum dot that emits between 6700 and 7100 cm^{-1} inside our photonic crystal roughly 1.5 μm below the surface. Due to the dispersion, when the quantum emitter emits in the surface defect light, the frequency sets the wave vector, and hence the direction of the light. In other words, the emission frequency determines the direction: At 7100 cm^{-1}, the angle with the x axis at $k_y = 0$ is 0°, while at 6700 cm^{-1} it is ±28°.

VI. CONCLUSIONS AND OUTLOOK

In this paper, we investigated the effect of a planar defect at the surface of a 3D photonic band-gap crystal on its optical properties. Using momentum-resolved reflectivity spectra of p-polarized light, we probed the surface defect waves that show up as a deep minimum inside the high reflectivity of the 3D band gap. By tracking the troughs versus optical frequency and reflected wave vectors, we mapped out the dispersion relations of the defect states. To further interpret our experiments, we theoretically calculated the dispersion relations using a supercell method in the plane-wave expansion, for which we selected modes based on symmetry and confinement properties expected for this Bloch mode inside a surface defect excited with p-polarized plane waves. The supercell calculations and experiments match very well and show a dispersion curve that decreases as a function of $|k_z|$, indicative of a backward-propagating wave, confirmed by finite-difference time-domain computer simulations.

We anticipate that our experimental methods may be readily applied to 2D photonic crystals, 2D photonic quasicrystals, other 3D photonic crystals, and other nanostructures, such as superlattices [80]. Momentum-resolved imaging provides a large dataset in a short amount of time, similarly to, e.g., hyperspectral imaging, and it highlights the effect of defects very clearly.

ACKNOWLEDGMENTS

We thank Manashee Adhikary, Cornelis Harteveld, and Geert-Jan Kamphuis for their help with the optical setup and the 3D samples, Bert Mulder, Maël Hubert, and

Devashish Sharma for discussions and help with the experiments, and William Wardley, Femius Koenderink, and Femi Ojambati for discussions on **k**-space imaging. This work was supported by the project "Self-Assembled Icosahedral Photonic Quasicrystals with a Band Gap for Visible Light" (OCENW.GROOT.2019.071) of the "Nederlandse Organisatie voor Wetenschappelijk Onderzoek" (NWO); NWO-TTW Perspectief program P15-36 "Free-form scattering optics" (FFSO) with TUE, TUD, ASML, Demcon, Lumileds, Schott, Signify, and TNO; NWO-TTW Perspectief program P21-20 "Optical coherence; optimal delivery and positioning" (OPTIC) in collaboration with TUE, TUD, and ARCNL, Anteryon, ASML, Demcon, JMO, Signify, and TNO; NWO JCSER Program, Project No. 680-91-084, "Accurate and Efficient Computation of the Optical Properties of Nanostructures for Improved Photovoltaics". W.L.V. wishes to dedicate this paper to the memory of Costas Soukoulis, one of the "fathers" of the inverse woodpile structure who greatly stimulated our research.

DATA AVAILABILITY

The data that support the findings of this article are openly available [81].

APPENDIX A: MORE INFORMATION ON THE RECIPROCAL SPACE

The coordinates of the high-symmetry points in the irreducible Brillouin zone of the body-centered tetragonal lattice are tabulated in Table I. The band structure for the photonic crystal is calculated along these high-symmetry points using the parameters from our experiments and is shown in Fig. 11.

TABLE I. Labels and corresponding positions along the irreducible Brillouin zone. The first set of positions are in the units of the lattice vectors, Eq. (2). The second set is coordinates in the Cartesian plane, for clarity divided by $2\pi/a$. The band structure is calculated along these points in this order.

Label	$\mathbf{b}_1$	$\mathbf{b}_2$	$\mathbf{b}_3$	k_x	k_y	k_z
M	$\frac{1}{2}$	$\frac{1}{2}$	$-\frac{1}{2}$	0	0	1
Γ	0	0	0	0	0	0
S_0	$-\frac{3}{8}$	$\frac{3}{8}$	$\frac{3}{8}$	$\frac{3\sqrt{2}}{4}$	0	0
S	$\frac{3}{8}$	$\frac{5}{8}$	$-\frac{3}{8}$	$\frac{\sqrt{2}}{4}$	0	1
M	$\frac{1}{2}$	$\frac{1}{2}$	$-\frac{1}{2}$	0	0	1
G	$\frac{1}{2}$	$\frac{1}{2}$	$-\frac{1}{4}$	$\frac{\sqrt{2}}{4}$	$\frac{\sqrt{2}}{4}$	1
S	$\frac{3}{8}$	$\frac{5}{8}$	$-\frac{3}{8}$	$\frac{\sqrt{2}}{4}$	0	1
N	0	$\frac{1}{2}$	0	$\frac{\sqrt{2}}{2}$	0	$\frac{1}{2}$
P	$\frac{1}{4}$	$\frac{1}{4}$	$\frac{1}{4}$	$\frac{\sqrt{2}}{2}$	$\frac{\sqrt{2}}{2}$	$\frac{1}{2}$
X	0	0	$\frac{1}{2}$	$\frac{\sqrt{2}}{2}$	$\frac{\sqrt{2}}{2}$	0
R	$-\frac{1}{4}$	$\frac{1}{4}$	$\frac{1}{2}$	$\frac{3\sqrt{2}}{4}$	$\frac{\sqrt{2}}{4}$	0
Γ	0	0	0	0	0	0
X	0	0	$\frac{1}{2}$	$\frac{\sqrt{2}}{2}$	$\frac{\sqrt{2}}{2}$	0

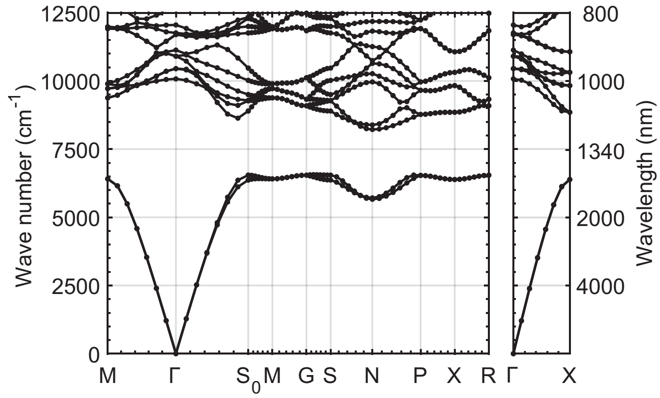

FIG. 11. Band structure (dispersion diagram) of a 3D photonic crystal with an inverse-woodpile structure. For this structure, the pore radius ($2r = d = 300$ nm) divided by the pitch ($a = 680$ nm) is equal to $r/a = 0.22$.

APPENDIX B: SYMMETRY ALONG THE PORES

To excite a Bloch mode with a certain incident wave, their symmetry properties must match [1]. There are many different Bloch modes with various symmetry properties. Here we restrict ourselves to waves with **k** vectors along $\Gamma S_0 M_0$, i.e., plane waves in the x direction.

As for the symmetry properties [82] of the Bloch modes, there are four symmetry possibilities, Σ_1 to Σ_4, along the $\Gamma S_0 M_0$ line [42]. As for the incident wave, s- and p-polarized plane waves are used in the laboratory. We will elaborate on which symmetries (Σ_1 to Σ_4) we can excite using s- and p-polarized plane waves.

Three symmetry operations determine the symmetry of a Bloch mode along $\Gamma S_0 M_0$. To start with, take the symmetry operation $\{2_{100}|0, 0, 0\}$, which rotates the electric field 180° around the x axis. From symmetry tables, we find that Σ_1 and Σ_2 states are symmetric for this operation, while Σ_3 and Σ_4 states are antisymmetric. Next imagine a plane wave with $\mathbf{k} = k_x\hat{\mathbf{x}}$ and the $\mathbf{E}$ field somewhere in the yz plane; see Fig. 12(a). The symmetry operation $\{2_{100}|0, 0, 0\}$ effectively flips the sign of the $\mathbf{E}$ field. Therefore, plane waves are always

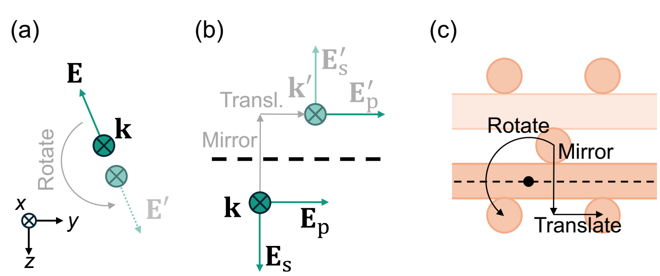

FIG. 12. (a) A plane wave with $\mathbf{k} = k_x\hat{\mathbf{x}}$, and an electric field perpendicular to that. $\mathbf{E}'$ is the result of the symmetry operation $\{2_{100}|0, 0, 0\}$ on $\mathbf{E}$. (b) An s- and p-polarized plane wave with $\mathbf{k} = k_x\hat{\mathbf{x}}$. $\mathbf{E}'$ is the result of the symmetry operation $\{m_{001}|0, \frac{1}{2}, 0\}$, which first mirrors in a z plane and then translates in the positive y direction. (c) The crystal maps to itself under the symmetry operations $\{2_{100}|0, 0, 0\}$ and $\{m_{001}|0, \frac{1}{2}, 0\}$. The black dot denotes $x = y = z = 0$.

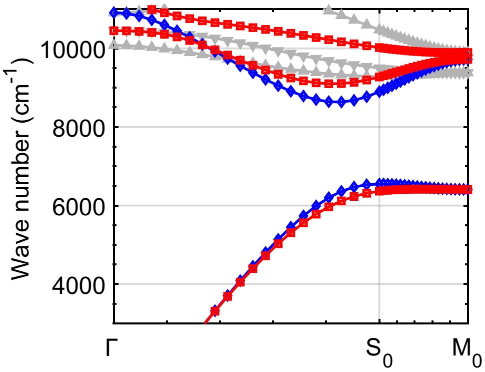

FIG. 13. Bands calculated along $\Gamma S_0 M_0$ with symmetry properties (blue diamonds) Σ_3, (red squares) Σ_4, (gray downwards triangles) Σ_1, and (gray upwards triangles) Σ_2. Calculated for pore diameter 300 nm. *s*-Polarized waves only excite Σ_3 modes, and *p*-polarized waves Σ_4 modes.

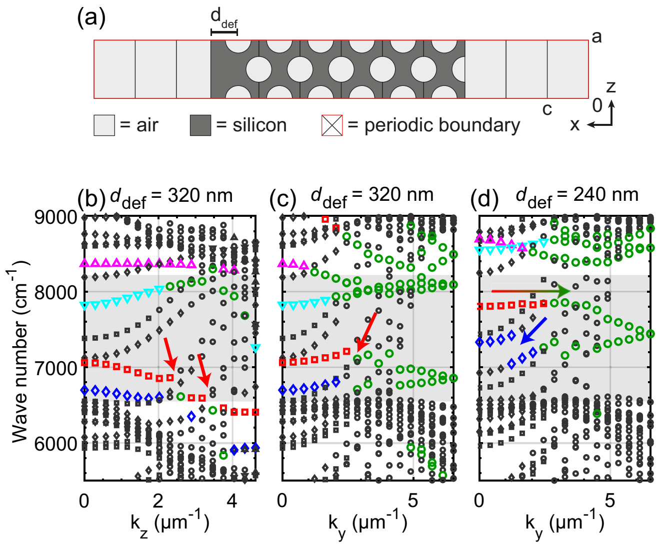

FIG. 14. (a) Schematic of the supercell in the *xz* plane. The pores along the *x* direction are omitted for clarity. There are six air blocks and six photonic crystal blocks. The leftmost photonic crystal block has $d_{def} = 320$ nm while the rightmost has proper surface termination. The red outline denotes that all boundaries are periodic. [(b)–(d)] Bloch modes calculated along the k_z and k_y directions using the supercell method. Gray: Calculated band gap. Black: Spurious air and bulk photonic crystal Bloch modes. Color: Modes in the surface defect layer. Downwards triangles, upwards triangles, diamonds, and squares correspond to Σ_1 to Σ_4, respectively. Circles have no categorized symmetry type. Red and blue arrows: Examples of points where the air modes interfere with the surface defect mode. Red to green arrow: Modes becoming less excitable by *p*-polarized plane waves, eventually below the threshold defined in the text.

antisymmetric for the $\{2_{100}|0, 0, 0\}$ operation, which means they can only excite Σ_3 or Σ_4 states.

The second symmetry operation of Bloch modes along the $\Gamma S_0 M_0$ line is $\{m_{001}|0, \frac{1}{2}, 0\}$, which is a mirror operation in the *z* plane, followed by a translation of half a unit cell in the *y* direction. According to the symmetry tables, Σ_3 is antisymmetric for this operation, while Σ_4 is symmetric. Whether a plane wave is symmetric or antisymmetric for this operation depends on the polarization of the plane wave. Take a plane wave with $\mathbf{k} = k_x\hat{\mathbf{x}}$ and the $\mathbf{E}$ field pointing in the $+z$ direction (*s*-polarized). Performing the operation $\{m_{001}|0, \frac{1}{2}, 0\}$ on this wave results in a $\mathbf{E}$ field that is pointing in the $-z$ direction, see Fig. 12(b), and thus the *s*-polarized wave is antisymmetric for this symmetry operation, just like Σ_3. On the contrary, a *p*-polarized wave has an $\mathbf{E}$ field in the *y* direction, which is symmetric for this symmetry operation, just like Σ_4. Note that the translation does not matter for the plane wave because $\mathbf{k} = k_x\hat{\mathbf{x}}$ is orthogonal to the translation.

The third symmetry operation, $\{m_{010}|0, \frac{1}{2}, 0\}$, does not provide additional constraints, and is therefore not detailed further.

As an example, in Fig. 12(c) the first and second symmetry operations are performed on one point, namely $x = 0$, $y = a/(4\sqrt{2})$, and $z = a/4$.

In summary, along the *x* direction, *s*-polarized (*p*-polarized) plane waves only excite modes in the Σ_3 (Σ_4) symmetry group. Besides, modes in the Σ_1 and Σ_2 groups cannot be excited with plane waves due to symmetry constraints. The bands along the $\Gamma S_0 M_0$ path are shown with their symmetry properties in Fig. 13.

APPENDIX C: SUPERCELL CALCULATION RESULTS

Using the supercell method, we calculate the frequency of the surface defect mode as a function of k_y and k_z. However, we also obtain the frequency of the spurious air and photonic crystal modes, which we wish to remove. The strategy of Ref. [70] to keep only the modes that do not shift when adjusting the number of cells requires many calculations and does not provide enough information here, so we use a different approach based on confinement and symmetry, which we will explain.

A surface mode represents energy confined near the surface. Therefore, we calculate the energy density of each mode and consider a mode to be confined near the surface if at least 50% of the mode's energy density is located within one unit cell about the surface. Additionally, as we only experimentally probe the crystal with *p*-polarized light, the symmetries of the calculated modes are also important. Although symmetry types are only defined for waves with exactly $\mathbf{k} = k_x\hat{\mathbf{x}}$, we define a *most-dominant* symmetry type for off-axis modes if their field is at least 50% symmetric or antisymmetric for all three symmetry operations described in Appendix B [83].

The Bloch modes from the supercell method calculated for a structure with $d_{def} = 320$ nm are shown in Figs. 14(b) and 14(c), where the red squares pertain to surface defect modes excited with predominantly *p*-polarized light, i.e., the modes that we can excite in our experiment. The calculated dispersion as a function of k_z is mostly smooth, but there is disturbance by the air modes between $k_z \in [2.31, 2.60]$ μm^{-1} and between $k_z \in [3.18, 3.46]$ μm^{-1}; see the red arrows in Fig. 14(b). We therefore disregard the states in those regions to obtain a good estimate of the dispersion as a function of k_z.

The disturbance is much stronger against k_y, where the surface mode is pushed up by a *p*-polarized air mode near

$k_y = 2\ \mu\text{m}^{-1}$ at the red arrow in Fig. 14(c). Near the same point, the mode becomes less excitable with incident p-polarized plane waves, eventually below the threshold defined earlier, i.e., it becomes uncategorized (green circles). As there are no confined modes between $7200\ \text{cm}^{-1} < \tilde{\nu} < 7800\ \text{cm}^{-1}$, we know that the mode should follow the uncategorized mode to $\tilde{\nu} = 6860\ \text{cm}^{-1}$. The calculated modes excitable by p-polarized light between $1\ \mu\text{m}^{-1} < k_y < 5\ \mu\text{m}^{-1}$ do not accurately describe the dispersion of the surface defect mode [84] (blue diamonds). The hybridization of the defect mode with the air mode is especially visible for $d_{\text{def}} = 240$ nm near $k_y = 1\ \mu\text{m}^{-1}$ (blue arrow). To obtain the shape of the mode, the same calculation is performed with $d_{\text{def}} = 240$ nm, where the defect mode excitable by p-polarized light is hardly disturbed by p-polarized air modes; see Fig. 14(d). Besides, the red squared data points clearly continue in the green circular data points. To obtain a good estimate of the dispersion of the surface mode as a function of k_y, we linearly scale the dispersion of the mode of $d_{\text{def}} = 240$ nm to the beginning and end point of the mode of $d_{\text{def}} = 320$ nm. The resulting dispersion as a function of k_z and k_y are shown in Fig. 9.

APPENDIX D: LIST OF MEASUREMENTS

In our study, we collected momentum-resolved reflectivity on two different structures, which were etched simultaneously on the same beam. All measurements are listed in Table II. We only show the first and second sets of measurements in this document, and of those, except for Fig. 6, only p-polarized light for the following reasons: (1) Crystal number 3 has smaller pores by design, leading to a band gap $100\ \text{cm}^{-1}$ lower than that of crystal 2 for p-polarized light, which is closer to the lower edge of our detection regime. The dispersion of crystal 3's surface defect has the same shape as crystal 2's, as is observed in the additional Supplemental Material videos Refs. [60,62]. (2) Waves incident from the x direction (y direction) are incident perpendicular to the first (second) etch direction. As the first etch step is less complex, the dispersion of the surface defect mode is more symmetric for momentum-resolved imaging from the x direction than the y direction. (3) The surface defect mode excitable with s-polarized light (blue diamonds in Fig. 14) is not as clear in experiment as the mode excitable with p-polarized light, probably because the frequency of the s-polarized mode is almost at the bottom of the band gap.

TABLE II. List of measurements performed for this paper.

Beam	Crystal number	Incidence axis	Surface defect	Maximum R (%)
15F	2	x	Present	75
15F	2	x	Absent	80
15F	2	y	Present	60
15F	2	y	Absent	64
15F	3	x	Present	79
15F	3	x	Absent	75
15F	3	y	Present	65
15F	3	y	Absent	68

APPENDIX E: MOMENTUM-RESOLVED SIMULATION

We provide a proof-of-principle simulation for the redirection of incident light toward the normal. The FDTD package MEEP [69] is used to simulate the momentum-resolved reflectivity of a 3D photonic crystal with an inverse woodpile structure without surface defect and, as a reference sample, the reflectivity of an empty space. The crystal has a size of $6c \times 6c \times 6a$ rectangular unit cells with $a = 680$ nm, $d_{\text{pore}} = 300$ nm, and a resolution of 29 pixels per μm. To enhance spatial resolution and increase the maximum source size, we add 4 μm of free space padding in the $\pm y$ and $\pm z$ directions.

A p-polarized Gaussian pulse, centered at $\tilde{\nu} = 7500\ \text{cm}^{-1}$ with a full width at half maximum of $\Delta\tilde{\nu} = 5000\ \text{cm}^{-1}$, is directed at the sample. The fields are recorded at a distance of 0.25 μm above the surface and then Fourier transformed as a function of $\tilde{\nu}$, k_y, and k_z to obtain the momentum-resolved amplitudes $\mathcal{F}\{A_{\text{phc}}\}$ and $\mathcal{F}\{A_{\text{empty}}\}$. The reflectivity as a function of wave number $\tilde{\nu}$ and transverse momenta k_y and k_z is computed as

$$R_{\text{phc}} = 100\% \,\frac{|\mathcal{F}\{A_{\text{phc}}\} - \mathcal{F}\{A_{\text{empty}}\}|^2}{|\mathcal{F}\{A_{\text{empty}}\}|^2}. \tag{E1}$$

As a source for the pulse, we use MEEP's default GaussianBeam3DSource. The intensity distribution of the source in this simulation does not resemble the experiment perfectly: In the experiment, each **k** vector has the same intensity up to a sharp cutoff by the objective's numerical aperture, whereas here the intensity has necessarily a Gaussian distribution. Therefore, the simulated results will differ quantitatively from the experiments. However, just like in the experiment, reflection of the simulated light from oblique angles to close to normal **k** vectors can lead to directional reflectivities R_{phc} into the normal direction of more 100%.

The simulated momentum-resolved reflectivity of the 3D photonic band-gap crystal is shown in Fig. 15, where we show

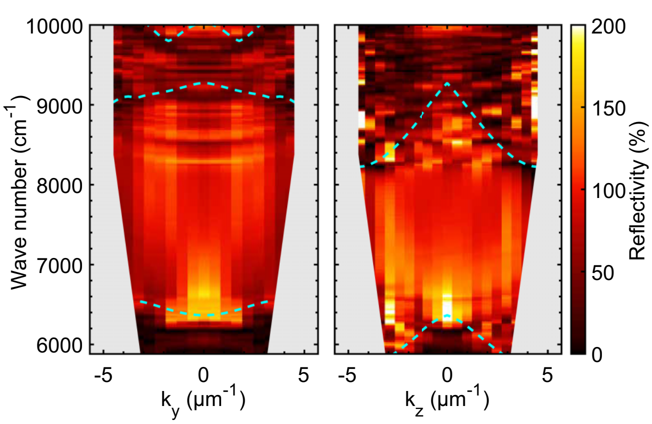

FIG. 15. Simulated momentum-resolved reflectivity R for p-polarized light of a 3D photonic band-gap crystal without surface defect $d_{\text{def}} = 0$. Gray area: Data are excluded because of numerical noise. Cyan dashed: Symmetry-selected bands calculated along the red and blue lines in Fig. 2(b) for pore diameter $d = 300$ nm.

cross sections at $k_z = 0$ and $k_y = 0$. We find high reflectivity in the band gap (red), which is bounded by the (cyan) calculated bands. In addition, we observe that the directional reflectivity towards the normal reaches values higher than 100% (yellow) at the lower side of the band gap $\tilde{\nu} = 6500$ cm^{-1}. This proof-of-principle simulation shows that this 3D photonic band-gap crystal reflects certain **k** vectors of a sharply focused incident beam toward the normal direction, such that in the normal direction, the directional reflectivity is higher than 100%. The results corroborate our observations in experiments.

[1] K. Sakoda, *Optical Properties of Photonic Crystals*, Springer Series in Optical Sciences Vol. 80 (Springer, Berlin, 2005).

[2] J. Joannopoulos, S. G. Johnson, J. Winn, and R. D. Meade, *Photonic Crystals: Molding the Flow of Light*, 2nd ed. (Princeton University Press, Princeton, NJ, 2008).

[3] J.-M. Lourtioz, H. Benisty, V. Berger, J.-M. Gérard, D. Maystre, A. Tchelnokov, and D. Pagnoux, *Photonic Crystals* (Springer, Berlin, 2008).

[4] Edited by M. A. Noginov, G. Dewar, M. W. McCall, and N. I. Zheludev, *Tutorials in Complex Photonic Media* (SPIE, Bellingham, WA, 2009).

[5] L. Novotny and B. Hecht, *Principles of Nano-optics*, 2nd ed. (Cambridge University, Cambridge, UK, 2012).

[6] Edited by M. Ghulinyan and L. Pavesi, *Light Localisation and Lasing: Random and Quasi-random Photonic Structures* (Cambridge University Press, Cambridge, UK, 2014).

[7] The dielectric constant $\varepsilon = \varepsilon' + i\varepsilon''$ is written as a sum of a real part $\varepsilon' = \mathrm{Re}\{\varepsilon\}$ and an imaginary part $\varepsilon'' = \mathrm{Im}\{\varepsilon\}$.

[8] M. van Exter and A. Lagendijk, Ultrashort surface-plasmon and phonon dynamics, Phys. Rev. Lett. **60**, 49 (1988).

[9] W. L. Barnes, A. Dereux, and T. W. Ebbesen, Surface plasmon subwavelength optics, Nature (London) **424**, 824 (2003).

[10] S. A. Maier *et al.*, *Plasmonics: Fundamentals and Applications* (Springer, New York, 2007), Vol. 1.

[11] B. E. A. Saleh and M. C. Teich, *Fundamentals of Photonics*, 3rd ed. (John Wiley & Sons, Hoboken, NJ, 2019).

[12] F. H. L. Koppens, D. E. Chang, and J. García de Abajo, Graphene plasmonics: A platform for strong light-matter interactions, Nano Lett. **11**, 3370 (2011).

[13] Photonic crystals are nanostructures with spatially periodic variations of the dielectric constant, with length scales a of the order of the wavelength of light: $a \simeq \lambda$.

[14] O. Takayama, A. A. Bogdanov, and A. V. Lavrinenko, Photonic surface waves on metamaterial interfaces, J. Phys.: Condens. Matter **29**, 463001 (2017).

[15] K. Ishizaki and S. Noda, Manipulation of photons at the surface of three-dimensional photonic crystals, Nature (London) **460**, 367 (2009).

[16] K. Ishizaki, K. Gondaira, Y. Ota, K. Suzuki, and S. Noda, Nanocavities at the surface of three-dimensional photonic crystals, Opt. Express **21**, 10590 (2013).

[17] T. F. Krauss, R. M. De La Rue, and S. Brand, Two-dimensional photonic-bandgap structures operating at near-infrared wavelengths, Nature (London) **383**, 699 (1996).

[18] T. Baba, N. Fukaya, and J. Yonekura, *Integrated Photonics Research* (Optica, Washington, DC, 1999), p. RTuE3.

[19] S. G. Johnson, S. Fan, P. R. Villeneuve, J. D. Joannopoulos, and L. A. Kolodziejski, Guided modes in photonic crystal slabs, Phys. Rev. B **60**, 5751 (1999).

[20] D. Sharma, S. B. Hasan, R. Saive, J. J. W. van der Vegt, and W. L. Vos, Enhanced absorption in thin and ultrathin silicon films by 3D photonic band gap back reflectors, Opt. Express **29**, 41023 (2021).

[21] S. Fan and J. D. Joannopoulos, Analysis of guided resonances in photonic crystal slabs, Phys. Rev. B **65**, 235112 (2002).

[22] A. Rosenberg, M. W. Carter, J. A. Casey, M. Kim, R. T. Holm, R. L. Henry, C. R. Eddy, V. Shamamian, K. Bussmann, S. Shi *et al.*, Guided resonances in asymmetrical GaN photonic crystal slabs observed in the visible spectrum, Opt. Express **13**, 6564 (2005).

[23] Y. Zhang, A. Chen, W. Liu, C. W. Hsu, B. Wang, F. Guan, X. Liu, L. Shi, L. Lu, and J. Zi, Observation of polarization vortices in momentum space, Phys. Rev. Lett. **120**, 186103 (2018).

[24] L. Chen, K. A. Morgan, G. A. Alzaidy, C.-C. Huang, Y.-L. D. Ho, M. P. Taverne, X. Zheng, Z. Ren, Z. Feng, I. Zeimpekis *et al.*, Observation of complete photonic bandgap in low refractive index contrast inverse rod-connected diamond structured chalcogenides, ACS Photon. **6**, 1248 (2019).

[25] S. Cueff, L. Berguiga, and H. S. Nguyen, Fourier imaging for nanophotonics, Nanophotonics **13**, 841 (2024).

[26] S. Foteinopoulou, M. Kafesaki, E. N. Economou, and C. M. Soukoulis, Backward surface waves at photonic crystals, Phys. Rev. B **75**, 245116 (2007).

[27] S. Foteinopoulou, G. Kenanakis, N. Katsarakis, I. Tsiapa, M. Kafesaki, E. N. Economou, and C. M. Soukoulis, Experimental verification of backward wave propagation at photonic crystal surfaces, Appl. Phys. Lett. **91**, 214102 (2007).

[28] A. P. Vinogradov, A. V. Dorofeenko, A. M. Merzlikin, and A. A. Lisyansky, Surface states in photonic crystals, Phys. Usp. **53**, 243 (2010).

[29] J. Hu, S. Tian, Y. Yang, S. Zhuang, and H. Guo, Dispersion engineering in unidirectional excitation of the surface wave of photonic crystal, Opt. Lett. **43**, 5319 (2018).

[30] D. Yilmaz, A. Yeltik, and H. Kurt, Highly controlled Bloch wave propagation in surfaces with broken symmetry, Opt. Lett. **43**, 2660 (2018).

[31] E. Gonzalez-Valencia, I. Del Villar, and P. Torres, Bloch waves at the surface of a single-layer coating D-shaped photonic crystal fiber, Opt. Lett. **45**, 2547 (2020).

[32] K. M. Ho, C. T. Chan, C. M. Soukoulis, R. Biswas, and M. Sigalas, Photonic band gaps in three dimensions: New layer-by-layer periodic structures, Solid State Commun. **89**, 413 (1994).

[33] M. Maldovan and E. L. Thomas, Diamond-structured photonic crystals, Nat. Mater. **3**, 593 (2004).

[34] L. A. Woldering, A. P. Mosk, R. W. Tjerkstra, and W. L. Vos, The influence of fabrication deviations on the photonic band gap of three-dimensional inverse woodpile nanostructures, J. Appl. Phys. **105**, 093108 (2009).

[35] J. M. van den Broek, L. A. Woldering, R. W. Tjerkstra, F. B. Segerink, I. D. Setija, and W. L. Vos, Inverse-woodpile photonic

band gap crystals with a cubic diamondlike structure made from single-crystalline silicon, Adv. Funct. Mater. **22**, 25 (2012).
[36] D. Devashish, S. B. Hasan, J. J. W. van der Vegt, and W. L. Vos, Reflectivity calculated for a three-dimensional silicon photonic band gap crystal with finite support, Phys. Rev. B **95**, 155141 (2017).
[37] S. B. Hasan, A. P. Mosk, W. L. Vos, and A. Lagendijk, Finite-size scaling of the density of states in photonic band-gap crystals, Phys. Rev. Lett. **120**, 237402 (2018).
[38] M. Adhikary, R. Uppu, C. A. M. Harteveld, D. A. Grishina, and W. L. Vos, Experimental probe of a complete 3D photonic band gap, Opt. Express **28**, 2683 (2020).
[39] S. R. Huisman, R. V. Nair, L. A. Woldering, M. D. Leistikow, A. P. Mosk, and W. L. Vos, Signature of a three-dimensional photonic band gap observed on silicon inverse woodpile photonic crystals, Phys. Rev. B **83**, 205313 (2011).
[40] To match with the symmetry tables, this notation differs from different work of our group where the pores were taken to be parallel to the x and z directions.
[41] T. Hahn, U. Shmueli, and J. C. W. Arthur, *International Tables for Crystallography* (Reidel, Dordrecht, 1983), Vol. 1.
[42] M. I. Aroyo, A. Kirov, C. Capillas, J. M. Perez-Mato, and H. Wondratschek, Bilbao crystallographic server. II. Representations of crystallographic point groups and space groups, Acta Crystallogr. A **62**, 115 (2006).
[43] K. Sakoda, Transmittance and Bragg reflectivity of two-dimensional photonic lattices, Phys. Rev. B **52**, 8992 (1995).
[44] S. Foteinopoulou and C. M. Soukoulis, Electromagnetic wave propagation in two-dimensional photonic crystals: A study of anomalous refractive effects, Phys. Rev. B **72**, 165112 (2005).
[45] D. A. Grishina, C. A. M. Harteveld, L. A. Woldering, and W. L. Vos, Method for making a single-step etch mask for 3D monolithic nanostructures, Nanotechnology **26**, 505302 (2015).
[46] M. J. Goodwin, C. A. M. Harteveld, M. J. de Boer, and W. L. Vos, Deep reactive ion etching of cylindrical nanopores in silicon for photonic crystals, Nanotechnology **34**, 225301 (2023).
[47] C. P. Mavidis, A. C. Tasolamprou, S. B. Hasan, T. Koschny, E. N. Economou, M. Kafesaki, C. M. Soukoulis, and W. L. Vos, The local density of optical states in the 3d band gap of a finite photonic crystal, Phys. Rev. B **101**, 235309 (2020).
[48] W. L. Vos and H. M. van Driel, Higher order Bragg diffraction by strongly photonic fcc crystals: Onset of a photonic bandgap, Phys. Lett. A **272**, 101 (2000).
[49] S. Noda, K. Tomoda, N. Yamamoto, and A. Chutinan, Full three-dimensional photonic bandgap crystals at near-infrared wavelengths, Science **289**, 604 (2000).
[50] M. J. A. de Dood, B. Gralak, A. Polman, and J. G. Fleming, Superstructure and finite-size effects in a Si photonic woodpile crystal, Phys. Rev. B **67**, 035322 (2003).
[51] M. Qi, E. Lidorikis, P. T. Rakich, S. G. Johnson, J. D. Joannopoulos, E. P. Ippen, and H. I. Smith, A three-dimensional optical photonic crystal with designed point defects, Nature (London) **429**, 538 (2004).
[52] W. Man, M. Megens, P. J. Steinhardt, and P. M. Chaikin, Experimental measurement of the photonic properties of icosahedral quasicrystals, Nature (London) **436**, 993 (2005).
[53] S. Takahashi, K. Suzuki, M. Okano, M. Imada, T. Nakamori, Y. Ota, K. Ishizaki, and S. Noda, Direct creation of three-dimensional photonic crystals by a top-down approach, Nat. Mater. **8**, 721 (2009).
[54] K. Suzuki, K. Ishizaki, Y. Ota, and S. Noda, Surface modes of three-dimensional photonic crystals constructed using a top-down approach, Opt. Express **19**, 25651 (2011).
[55] N. Le Thomas, R. Houdré, M. V. Kotlyar, D. O'Brien, and T. F. Krauss, Exploring light propagating in photonic crystals with Fourier optics, J. Opt. Soc. Am. B **24**, 2964 (2007).
[56] Y. Zhang, M. Zhao, J. Wang, W. Liu, B. Wang, S. Hu, G. Lu, A. Chen, J. Cui, W. Zhang, C. W. Hsu, X. Liu, L. Shi, H. Yin, and J. Zi, Momentum-space imaging spectroscopy for the study of nanophotonic materials, Sci. Bull. **66**, 824 (2021).
[57] Y. Zhang, Z. Che, W. Liu, J. Wang, M. Zhao, F. Guan, X. Liu, L. Shi, and J. Zi, Unfolded band structures of photonic quasicrystals and moiré superlattices, Phys. Rev. B **105**, 165304 (2022).
[58] R. Uppu, M. Adhikary, C. A. M. Harteveld, and W. L. Vos, Spatially shaping waves to penetrate deep inside a forbidden gap, Phys. Rev. Lett. **126**, 177402 (2021).
[59] See Supplemental Material at http://link.aps.org/supplemental/10.1103/jckd-3l5d for a video of the 3D dataset of momentum-resolved reflectivity on bar 15F crystal 2 without surface defect.
[60] See Supplemental Material at http://link.aps.org/supplemental/10.1103/jckd-3l5d for a video of the 3D dataset of momentum-resolved reflectivity on bar 15F crystal 2 with a surface defect.
[61] See Supplemental Material at http://link.aps.org/supplemental/10.1103/jckd-3l5d for a video of the 3D dataset of momentum-resolved reflectivity on bar 15F crystal 3 without surface defect.
[62] See Supplemental Material at http://link.aps.org/supplemental/10.1103/jckd-3l5d for a video of the 3D dataset of momentum-resolved reflectivity on bar 15F crystal 3 with a surface defect.
[63] A complete study of all refraction effects requires equifrequency surfaces, which also enable further analysis of the excitation of Bloch modes by a particular $\mathbf{k}_{\text{in}}$ from the direction of the group velocity Refs. [2,44].
[64] S. G. Johnson and J. D. Joannopoulos, Block-iterative frequency-domain methods for maxwell's equations in a planewave basis, Opt. Express **8**, 173 (2001).
[65] L. Elcoro, B. Bradlyn, Z. Wang, M. G. Vergniory, J. Cano, C. Felser, B. A. Bernevig, D. Orobengoa, G. de la Flor, and M. I. Aroyo, Double crystallographic groups and their representations on the Bilbao crystallographic server, J. Appl. Crystallogr. **50**, 1457 (2017).
[66] The wave number $\tilde{\nu} = \omega/2\pi c_0$ is in spectroscopic tradition gauged in cm^{-1} that is equivalent to the older unit kayser Ref. [85].
[67] M. Notomi, Theory of light propagation in strongly modulated photonic crystals: Refractionlike behavior in the vicinity of the photonic band gap, Phys. Rev. B **62**, 10696 (2000).
[68] Bloch modes inside the infinite photonic crystal adhere to the Laue condition: A Bloch mode with wave vector $\mathbf{k}'$ is equivalent to one with wave vector $\mathbf{k}' + \mathbf{G}$.
[69] A. F. Oskooi, D. Roundy, M. Ibanescu, P. Bermel, J. D. Joannopoulos, and S. G. Johnson, Meep: A flexible free-software package for electromagnetic simulations by the FDTD method, Comput. Phys. Commun. **181**, 687 (2010).
[70] R. D. Meade, K. D. Brommer, A. M. Rappe, and J. D. Joannopoulos, Electromagnetic Bloch waves at the surface of a photonic crystal, Phys. Rev. B **44**, 10961 (1991).

[71] R. Hillebrand, S. Senz, W. Hergert, and U. Gösele, Macroporous-silicon-based three-dimensional photonic crystal with a large complete band gap, J. Appl. Phys. **94**, 2758 (2003).

[72] J. Schilling, J. White, A. Scherer, G. Stupian, R. Hillebrand, and U. Gösele, Three-dimensional macroporous silicon photonic crystal with large photonic band gap, Appl. Phys. Lett. **86**, 011101 (2005).

[73] F. García-Santamaría, M. Xu, V. Lousse, S. Fan, P. V. Braun, and J. A. Lewis, A germanium inverse woodpile structure with a large photonic band gap, Adv. Mater. **19**, 1567 (2007).

[74] Resonant modes and transmission in a waveguide cavity, http://meep.readthedocs.io/en/latest/Python_Tutorials/Resonant_Modes_and_Transmission_in_a_Waveguide_Cavity/#band-diagram, accessed 22-November-2024).

[75] See Supplemental Material at http://link.aps.org/supplemental/10.1103/jckd-3l5d for a video of the simulations of Fig. 8.

[76] L. J. Corbijn van Willenswaard, S. Smeets, N. Renaud, M. Schlottbom, J. J. W. van der Vegt, and W. L. Vos, Non-utopian optical properties computed of a tomographically reconstructed real photonic nanostructure, Opt. Express **32**, 32028 (2024).

[77] ε_3' was estimated from our FDTD simulations from the gradient of the electric field strength into the bulk of the band gap crystal (cf. Fig. 8). It turns out that the precise value of ε_3' is not critical, as long as $\varepsilon_3' \ll \varepsilon_2'$.

[78] A. F. Koenderink, Emission and transport of light in photonic crystals, Ph.D. thesis, Universiteit van Amsterdam, 2003.

[79] M. Born and E. Wolf, *Principles of Optics: Electromagnetic Theory of Propagation, Interference and Diffraction of Light*, 7th ed. (Cambridge University Press, Cambridge, UK, 2013).

[80] S. A. Hack, J. J. W. van der Vegt, and W. L. Vos, Cartesian light: Unconventional propagation of light in a three-dimensional superlattice of coupled cavities within a three-dimensional photonic band gap, Phys. Rev. B **99**, 115308 (2019).

[81] T. J. Vreman, M. J. Goodwin, L. J. Corbijn van Willenswaard, W. J. Barnes, A. Lagendijk, and W. L. Vos, [Dataset], Zenodo (2025), https://doi.org/10.5281/zenodo.14845289.

[82] The symmetry properties of Bloch modes follow from the irreducible representations of the group of the wave vector. The given wave vectors are on the Σ high symmetry line for which there are four irreducible representations: Σ_1 to Σ_4.

[83] Just like Bloch modes of the bulk structure, Bloch modes in the surface defect wave have an energy density that is mostly present in a structure with space symmetry group 141. Therefore, we expect that the symmetry of the bulk PC bands and the surface defect mode are not much different, and we use the same symmetry matrices for the modes of the bulk PC as for the surface defect modes.

[84] To provide an additional example, the effect of the disturbance of air modes with a surface mode is clearer for the modes excitable by *s*-polarized light.

[85] Wikipedia contributors, Wavenumber, Wikipedia https://en.wikipedia.org/w/index.php?title=Wavenumber&oldid=1235416429.